Characterisation of a laser plasma betatron source for high resolution x-ray imaging

OPEN ACCESS
IOP Publishing
Plasma Physics and Controlled Fusion
Plasma Phys. Control. Fusion **63** (2021) 084010 (7pp)
https://doi.org/10.1088/1361-6587/ac0fcf

Characterisation of a laser plasma betatron source for high resolution x-ray imaging

O J Finlay[1,2,*], J-N Gruse[3], C Thornton[4], R Allott[4], C D Armstrong[4], C D Baird[5], N Bourgeois[4], C Brenner[4], S Cipiccia[6,12], J M Cole[3], C Gregory[4], S Jamison[1,2], Y Katzir[4], N C Lopes[3,7], S P D Mangles[3], C D Murphy[5], Z Najmudin[3], D Neely[4,13*], L R Pickard[8], K D Potter[9], P P Rajeev[4], D Rusby[4,10], M P Selwood[5], D R Symes[4], C I D Underwood[5], J C Wood[3], A G R Thomas[1,2,11,*] and M J V Streeter[1,2,3,*]

[1] The Cockcroft Institute, Keckwick Lane, Daresbury WA4 4AD, United Kingdom
[2] Physics Department, Lancaster University, Lancaster LA1 4YB, United Kingdom
[3] The John Adams Institute for Accelerator Science, Imperial College London, London SW7 2AZ, United Kingdom
[4] Central Laser Facility, STFC Rutherford Appleton Laboratory, Didcot OX11 0QX, United Kingdom
[5] York Plasma Institute, Department of Physics, University of York, York YO10 5DD, United Kingdom
[6] Diamond Light Source, Harwell Science and Innovation Campus, Fermi Avenue, Didcot OX11 0DE, United Kingdom
[7] GoLP/Instituto de Plasmas e Fusão Nuclear, Instituto Superior Técnico, U.L., Lisboa 1049-001, Portugal
[8] National Composites Centre, Bristol and Bath Science Park, Feynman Way Central, Emersons Green, Bristol BS16 7FS, United Kingdom
[9] Advanced Composites Collaboration for Science and Innovation (ACCIS), University of Bristol, Bristol BS8 1TR, United Kingdom
[10] Lawrence Livermore National Laboratory, Livermore, CA 94550, United States of America
[11] Center for Ultrafast Optical Science, University of Michigan, Ann Arbor, MI 48109-2099, United States of America
[12] Department of Medical Physics and Biomedical Engineering, University College London, Gower Street, London, UK

E-mail: oliver.finlay@cockcroft.ac.uk, agrt@umich.edu and m.streeter@qub.ac.uk

Received 25 January 2021, revised 15 March 2021
Accepted for publication 29 June 2021
Published 13 July 2021

Abstract

We report on the characterisation of an x-ray source, generated by a laser-driven plasma wakefield accelerator. The spectrum of the optimised source was consistent with an on-axis synchrotron spectrum with a critical energy of $13.8^{+2.2}_{-1.9}$ keV and the number of photons per pulse generated above 1 keV was calculated to be $6^{+1.2}_{-0.9} \times 10^9$. The x-ray beam was used to image a resolution grid placed 37 cm from the source, which gave a measured spatial resolution of 4 μm $\times$ 5 μm. The inferred emission region had a radius and length of 0.5 ± 0.2 μm and 3.2 ± 0.9 mm respectively. It was also observed that laser damage to the exit aperture of the gas cell led to a reduction in the accelerated electron beam charge and a corresponding reduction in x-ray flux due to the change in the plasma density profile.

[13] Author is deceased.
[*] Authors to whom any correspondence should be addressed.

Keywords: LWFA, betatron radiation, x-ray imaging, x-ray source characterisation, radiograph, plasma acceleration

(Some figures may appear in colour only in the online journal)

1. Introduction

Laser-driven plasma wakefield acceleration (LWFA) [1] is an established technique for the acceleration of electrons over very short distances [2–4]. Accelerated electrons can reach GeV scale energies in just a few millimeters, while transverse oscillations of the electron beams results in a bright femtosecond pulse of multi-keV x-rays [5]. As such LWFA x-ray sources have many near term applications [6], so the optimisation of the properties of these sources is an active area of study.

The ponderomotive force of a short, intense laser pulse travelling though a plasma drives electrons away from regions of high intensity, creating a region of net positive charge. The electrostatic force then attracts the electrons back to their equilibrium positions and they begin to oscillate at a characteristic plasma frequency, $\omega_p = \sqrt{n_e e^2/m_e \epsilon_0}$ where n_e is the plasma electron density. In the case of a strongly relativistic laser pulse, defined by a normalised vector potential $a_0 \gg 1$, almost all electrons are expelled from the centre of the pulse [7]. An approximately spherical ion cavity is formed in the wake of the laser, which propagates at the reduced group velocity of the laser in the plasma, $v_g/c = 1 - \frac{3}{2}(\omega_p/\omega_0)^2$ [8] where ω_0 is the angular frequency of the laser. The accelerating electric field in a laser wakefield accelerator can be estimated using the wave breaking limit for a cold non-relativistic plasma wave, $E_{\mathrm{wb}} = cm_e\omega_p/e$ [9]. From this it can be calculated that acceleration gradients on the order of 100 GeV m^{-1} can be generated at a density of $n_e \sim 10^{18}$ cm^{-3}.

Due to the sub-luminal group velocity of the driving laser pulse and the strong accelerating force, electrons are quickly accelerated to $\gamma \gg 1$ and so de-phase relative to the accelerating region of the wake [10]. For a constant value $a_0 \gg 1$, the distance travelled by the electron in the time over which this dephasing takes place is given by [8] $k_p L_\phi = \frac{4}{3}\sqrt{a_0}{\omega_0}^2/{\omega_p}^2$ where $k_p = \omega_p/c$ is the plasma wave number. From this it can be seen that $L_\phi \propto n_e^{-3/2}$. The final maximum electron energy that can obtained under these conditions can be estimated as $W_{\mathrm{max}} = (2/3)a_0(\omega_0/\omega_p)^2 m_e c^2$ [8], with the assumption that the electron is accelerated for a length $L_{\mathrm{acc}} = L_\phi$ in a non-evolving accelerating structure.

The accelerated electrons emit synchrotron radiation [11] as they oscillate in the focusing fields of the LWFA [5, 12, 13]. The radiation source is defined by the betatron strength parameter, α_β, which equals [14],

$$\alpha_\beta = r_\beta k_p \gamma_e, \tag{1}$$

where r_β is the betatron oscillation radius and $\gamma_e m_e c^2$ is the electron energy. The betatron parameter for a plasma source is equivalent to the deflection parameter, K, for conventional undulators/wigglers. Generally, sources with $\alpha_\beta < 1$ are known as undulators and sources with $\alpha_\beta > 1$ as wigglers. The transverse electron motion in current LWFA experiments corresponds to $\alpha_\beta \sim 10$ [15] which is described by the wiggler regime.

Assuming that the laser dimensions are matched to the plasma blowout radius and that the interaction length is equal to the dephasing length, the energy radiated by a single electron in an LWFA can be estimated as,

$$E_{\mathrm{rad}} = \frac{\pi^{3/2}}{2}\gamma_p^{7/2} a_0^5 m_e c^2, \tag{2}$$

where γ_p is the associated Lorentz factor of the bubble [5]. Given that current LWFA experiments operate in the wiggler regime, the on-axis spectrum can be approximated by a synchrotron spectrum of the form $S(E) = (\xi \mathcal{K}_{2/3}(\xi))^2$, where $\xi = \omega/2\omega_c$ is the emitted photon energy normalised to twice the critical frequency which characterises the spectrum. The critical frequency is given by [16],

$$\omega_{\mathrm{c}} = 3\ \alpha_\beta \gamma_{\mathrm{e}}^2 \omega_\beta, \tag{3}$$

where ω_β is the betatron frequency. For the experimental parameters considered in this paper, the critical energy, $E_c = \hbar\omega_c$, is on the order of tens of keV. These x-rays can be used for both medical [17, 18] and industrial [19, 20] radiography to image micron-scale features in the internal structure of a material in a single shot of the drive laser. The beam is spatially coherent after a few cm due to the micron-scale transverse size of the x-ray source, which allows phase contrast imaging to be performed. This can be exploited to reveal the internal structure of low-Z objects [13].

In the experiment reported here, the generated x-ray signal from an LWFA was optimised through control of the plasma density in a single stage gas cell. The imaging resolution of the optimised source was then characterised for application to the imaging of industrial samples [19]. In addition, the effects of gradual damage sustained by the plasma source during operation were investigated.

2. Experimental setup

The experiment was setup as shown in figure 1 using the Gemini laser at the Central Laser Facility. Each pulse contained 7.2 ± 0.4 J and had a full width half maximum (FWHM) duration of 49 ± 3 fs and a central wavelength of 800 nm. The laser pulses were focused using an f/40 off-axis parabola to a focal spot of FWHM size 50 μm $\times$ 40 μm. At the focus in vacuum, the laser had a peak normalised vector potential of $a_0 \approx 1.6$. The focus was aligned to the entrance aperture of a helium filled gas cell, in which it ionised the gas and drove the LWFA. The gas cell length used for optimisation of the plasma betatron source was 18 mm.

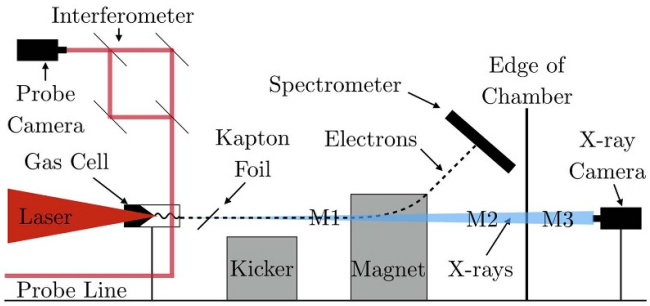

Figure 1. Simplified schematic of the experimental setup. The laser was focused at the gas cell entrance to drive the wake. The electron energy was calculated using the projection of the electrons onto a scintillating screen after being deflected by a magnetic field. An indirect detection x-ray camera captured radiographic images of samples which could be imaged at either M1, M2 or M3 to give different geometric magnifications. The interferometric image from the probe camera was used to calculated the gas cell density. The kapton foil was used to reflect the drive laser light toward a beam dump and the kicker magnet could be moved into the electron beam path to deflect the electrons away from a sample if imaging at M1.

The electron spectrometer used a Lanex scintillating screen to detect the accelerated electrons. A dipole magnet deflected electrons to different positions on the screen depending on their energy. The spectrometer was able to detect electrons with energies between 100 MeV and 2 GeV.

The x-ray camera used was an Andor iKon L 936 indirect detection camera which consists of a CCD camera fibre-coupled to a structured 150 μm thick caesium iodide scintillator, allowing the detection of high energy photons. The CCD was composed of 2048 $\times$ 2048 pixels, each a square of size 13.5 μm. Objects to be imaged could be placed at one of three different positions—M1, M2 or M3—along the beam line to give magnifications of 10.2, 2.2 or 1.5 respectively. M1, M2, M3 and the camera were 0.37, 1.6, 2.6 and 3.8 m away from the source respectively.

An array of various thin elements was used to determine the critical energy of the x-ray spectrum by an iterative fitting procedure [13]. The signal counts seen by the detector C is given by,

$$C = \alpha N_p \int_0^\infty S(E)\, Q(E)\, T(E)\, \mathrm{d}E\,, \tag{4}$$

where $Q(E)$ is the quantum efficiency of the camera, T is the combined transmission function of the elements in the beam path, N_p is the number of photons within the detection window, and α is a camera dependent calibration constant. The critical energy was determined by fitting the observed signal behind each filter, normalised to the signal with no added elements. The error in the inferred critical energy was due to a combination of the error in the measured filter thicknesses and the accuracy of fitting for the incident x-ray beam profile, which was used to calculate the transmission of each filter. To quantify this on a single shot, the fitting procedure was repeated with random element thicknesses within the given tolerance and with a random signal through each element within a range set by the residuals of the background beam profile fit. The total number of photons per pulse above a threshold energy was then calculated by integrating figure 4 over the spectrum defined by the retrieved critical energy. Figure 4 also suggests two approaches to maximising the signal seen by the camera: increasing the number of photons and choosing an optimal source spectrum for the given imaging system.

The gas density, and therefore the plasma density, was varied by changing the backing pressure of the gas injected into the cell. The plasma density for a given shot was measured from the phase shift seen by the probe interferometer. A small fraction of laser transmission through a dielectric mirror was used to probe the gas cell transversely immediately after the plasma channel had been formed by the main beam. A Mach–Zehnder interferometer was used to interfere different parts of the same beam in order to distinguish the plasma channel. Since the refractive index of the plasma is lower than the surrounding neutral gas, a phase shift can be seen in the interferogram. Due to intensity fluctuations of the incident probe beam, image filtering processes were used to determine the spatial variation in phase difference between the two beam replicas. A Fourier filter was used in conjunction with a Hilbert transform based phase retrieval method [21, 22] to extract the desired frequency components of the data. With the assumption of cylindrical symmetry, an Abel inversion was applied to the retrieved phase shift profile, $\Delta\phi$, to give a radial density profile,

$$n_e(z,r) = \frac{4\, m_e \epsilon_0 c^2}{\lambda_0 e^2} \int_r^\infty \mathrm{d}\Delta\phi y \frac{1}{\sqrt{y^2 - r^2}} \mathrm{d}y, \tag{5}$$

where z is the pump laser axis and y is the axis transverse to the pump laser and the probe light propagation. The plasma density was calculated by taking the average density along the central few pixels in the radial axis. This method was used to find a calibration between plasma density and gas backing pressure.

3. Optimisation of the x-ray source with respect to density

Figure 2 shows typical angularly resolved electron spectra for different plasma densities. For lower plasma densities, $n_e < 3 \times 10^{18}$ cm^{-3}, the electron beams exhibited a small angular divergence, on the order of $\sim$2 mrad. For plasma electron densities of 3.5 $\times$ 10^{18} cm^{-3} and 4.4 $\times$ 10^{18} cm^{-3}, the divergence of the electron beams increased dramatically.

The electron beam charge and maximum energy measured by the spectrometer were averaged over several shots, and are plotted in figure 3. The maximum electron energy gain occurs at a plasma density of 2.7 $\times$ 10^{18} cm^{-3}. As density increases, the dephasing length decreases, as described earlier, which limits energy gain. The energy gain for the lowest density does not follow this trend. This is because self-injection occurs later within the gas cell for lower densities, which means the acceleration length can be truncated by the end of the gas cell rather than the dephasing length [23]. The highest electron bunch charge was seen at a plasma density of

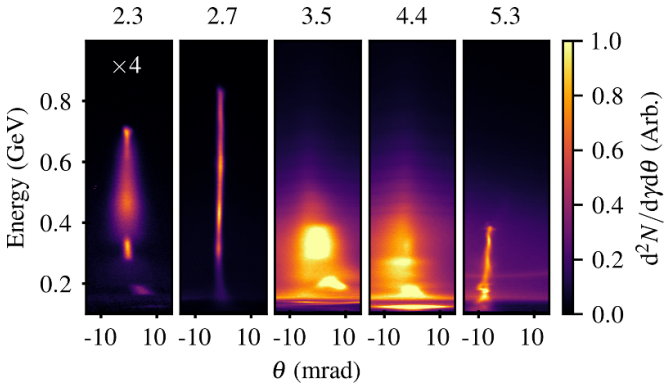

Figure 2. Angularly resolved electron spectra for different plasma densities. The plasma density given on top of each image is given in units of 10^{18} cm^{-3}. The spectrum in the left-most panel has been multiplied by 4 to make it visible on the same colour scale.

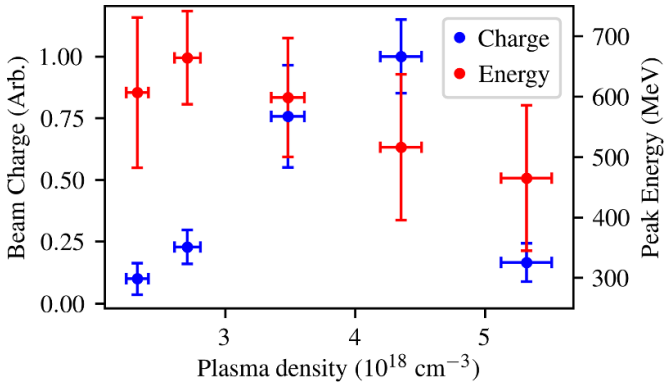

Figure 3. Dependence of the electron bunch charge and maximum electron energy on the plasma density. Each point shows the mean and standard deviation of between 16 and 21 electron spectra.

$(4.4 \pm 0.2) \times 10^{18}$ cm^{-3}. A precise charge measurement was not available in this experiment but in [17], with similar experimental conditions, an average bunch charge exceeding 100 pC was observed.

The exit aperture of the gas cell is particularly susceptible to damage from the residual laser pulse of the LWFA. Any of the laser energy that is not guided in the central filament can hit the inside of the exit aperture plate causing it to steadily widen. One major effect of the increased aperture size was to reduce the plasma density for a given input pressure. This is discussed in further detail in section 5. Although this could be compensated by increasing the input pressure, there was still a large decrease in performance for the damaged cell, as indicated by the differing x-ray beam characteristics in figure 4.

The integrated x-ray signal measured at different plasma densities is shown in figure 4(a). This signal is proportional to the energy deposited in the detector by x-ray photons. Using the damaged cell, the signal scales in a similar manner with respect to the plasma density as the electron bunch charge, and the highest x-ray signal coincided with the plasma density at which the highest electron bunch charge was observed. The

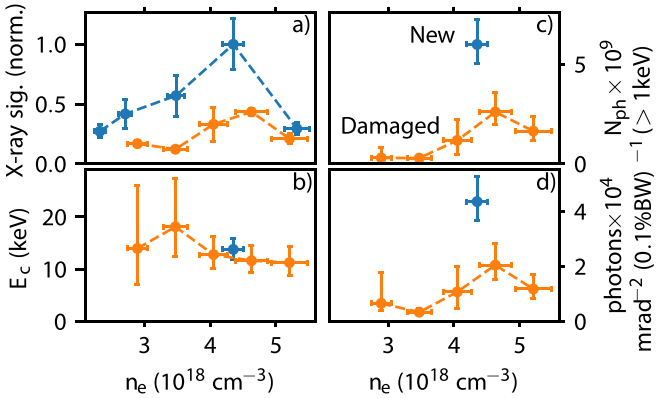

Figure 4. (a) Normalised total x-ray detector signal, (b) synchrotron spectrum critical energy, (c) number of photons per pulse above 1 keV and (d) peak spectral intensity per solid angle, all as functions of plasma density. The orange markers show results for a damaged gas cell (run 6 in figure 6) while the blue show results for a repaired cell (run 7 in figure 6) with a new exit aperture plate. Note, the critical energy and photon yield were only diagnosed at a single density for the newly repaired gas cell. Error bars include the measurement uncertainties and the standard error from averaging multiple shots.

Table 1. Table showing the electron and x-ray properties for a similar plasma density before and after the gas cell exit cone was changed.

	Damaged gas cell	New gas cell
Optimal density (10^{18} cm^{-3})	4.6 ± 0.2	4.4 ± 0.2
Average electron beam max energy (MeV)	450 ± 40	520 ± 120
Average electron beam charge (arb. units)	0.51 ± 0.11	1.00 ± 0.15
E_c (keV)	$11.6^{+2.9}_{-2.3}$	$13.8^{+2.2}_{-1.9}$
$N_{ph}/10^9$ (>1 keV)	$2.6^{+1.0}_{-0.6}$	$6.0^{+1.2}_{-0.9}$
Spectral intensity/10^4 (ph (0.1% BW)$^{-1}$ mrad^{-2})	$2.0^{+0.8}_{-0.5}$	$4.4^{+0.9}_{-0.7}$

difference in signal between the new and the damaged cell can be explained by the difference in bunch charge, as shown later in table 1.

The retrieved critical energy E_c of the on-axis synchrotron spectrum emitted by the source is shown in figure 4(b). This shows that the critical energy is higher at densities just above the injection threshold, where the observed maximum electron energy is also higher. The highest critical energy was $E_c = 18$ keV for $n_e = 3.5 \times 10^{18}$ cm^{-3}. The critical energy reduced with increasing plasma density, falling to 11.6 keV at the density at which the highest x-ray signal was observed. The total number of photons per pulse with energies above 1 keV (figure 4(c)) was found using figure 4 with the retrieved spectrum and by integrating the fit to the beam profile, which was observed in the regions between filters. The peak spectral flux of the x-ray source (figure 4(d)) was found by taking the peak of the fitted beam profile. Both of these

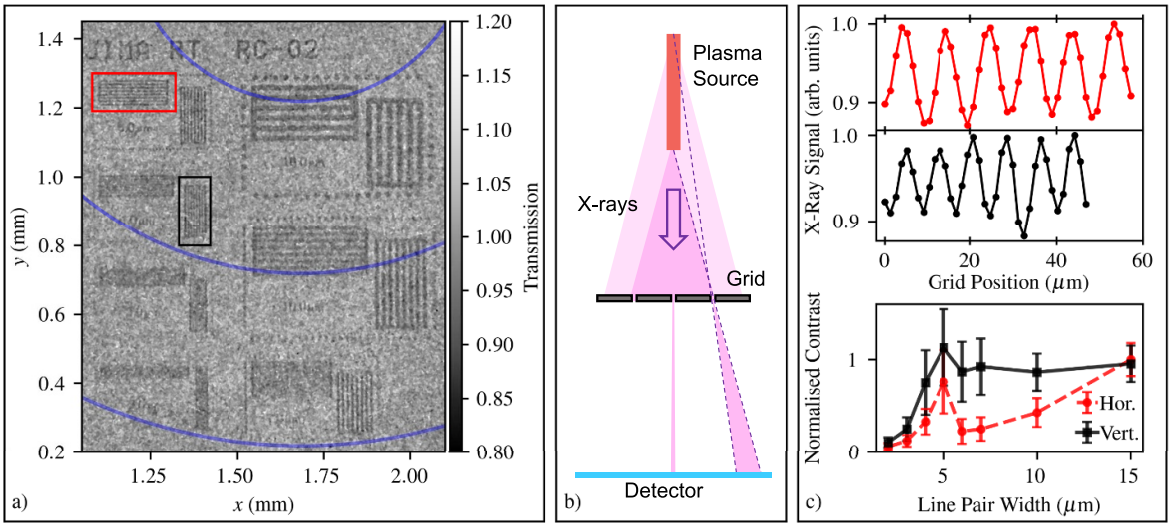

Figure 5. (a) Radiographic image of a JIMA resolution grid. The red and black boxes highlight the smallest resolved features. The blue circles indicate the central axis of the x-ray beam. (b) An illustration of the x-ray imaging geometry, showing how source length contributes to observed contrast for off-axis illumination. (c) (Top) Observed signal modulations for the grid sections highlighted in (a) for a single shot and (Bottom) the contrast transfer functions normalised to the measured contrast for the largest line-spacing for horizontal (red) and vertical (black) line pairs. Plot shows a mean and standard deviation of 21, single shot contrast functions.

quantities were maximised when the x-ray signal was highest and corresponded to the plasma density at which the most electron beam charge was observed.

For the new cell, the critical energy was only measured for the density which gave the maximum x-ray signal. This gave a slightly higher value than the neighbouring points of the damaged gas cell (although within errors) of $E_c = 13.8$ keV. This indicates that the spectral shape of the x-ray beams produced by the damaged cell is not significantly different from that produced with a fresh cell. This is consistent with the maximum electron beam energy measured using the new gas cell and the damaged cell being similar, as presented in table 1.

Figures 4(c) and (d) show that the number and peak flux of photons in the x-ray beams is dramatically affected by damage to the gas cell. At the optimal plasma density for x-ray signal, the number of photons increased by a factor of 2.3, while the peak spectral intensity increased by 2.1.

4. X-ray imaging with the optimised source

The resolution of this source was found by radiographically imaging a JIMA resolution grid [24], shown in figure 5(a). The smallest resolvable feature in a single shot horizontally was $\sim$4 μm, whilst the resolution limit vertically was $\sim$5 μm. The grid was 37 cm from the source and was imaged at a geometric magnification of $M \approx 10$, which gave an effective pixel size of 1.35 μm. The pointing fluctuation in the x-ray beam centroid was 0.7 mrad rms.

Line-outs of the smallest resolved line-pairs and contrast transfer functions (CTFs) for both the horizontal and vertical line-pairs can be seen in figure 5(c). The CTF for the vertical line-pairs displays a sharp decrease in contrast for the smaller line-pair widths as would be expected. The horizontal CTF however follows a more complicated trend. The contrast depends not only on the line-pair width, but also the position of the line-pairs with respect to the centre of the beam. This is because the x-ray emission region has a finite length, as well as a finite transverse size, which when imaging a sample off the beam axis at high magnification can be a limitation on the total image resolution, as shown in figure 5(b). This effectively increases the transverse source size along the axis of displacement from beam centre. For the image in figure 5(a), the source size increase is measured by the horizontal line-pairs when the vertical distance to the beam centre is significant, whereas the measured vertical line-pair contrast is affected by the horizontal distance to the centre of the x-ray beam. Since the x-ray beam was more often centred above the resolution grid, the effect of the longitudinal source size is more obvious in the CTF of the horizontal line-pairs.

The dimensions of the source volume were estimated by fitting the observed CTFs with the geometrical effects caused by a uniformly emitting cylinder aligned to the brightest region of the observed x-ray beam [13, 25]. Rays were traced from points within this cylindrical volume to each pixel of a synthetic detector. The intersection of each ray with the JIMA grid plane was calculated to determine if it hit the opaque or transmissive region of the grid, and only those which intersected the transmissive part contributed to the total signal of each pixel. The CTF was then calculated from the simulated image in the same way as the experimental data and the best fit for the source dimensions was found through iterative optimisation. For 21 shots, the average and standard deviation of the fitted radius and length of the emission region was 0.5 ± 0.2 μm $\times$ 3.2 ± 0.9 mm.

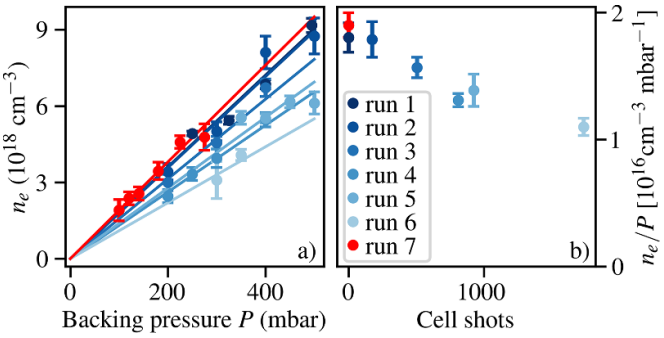

Figure 6. (a) Backing pressure to plasma density calibrations for each run and (b) as a function of number of shots on the gas cell during the experiment. The gas cell exit cone was replaced before run 7.

5. Effects of gas cell damage

The brass exit plate to the gas cell had a conical shape with an aperture at the tip. The thickness of the plate was ≈ 40 μm around the circumference of the hole. Throughout the experiment, the exit aperture sustained damage from the laser making it increase in size — from a few hundred μm to around 3 mm. The entrance aperture remained unaffected, since the laser pulse was always focused at this plane. As the exit aperture increased in size, a higher backing pressure had to be used to achieve the same average plasma densities. The deterioration of the cell was monitored by measuring the backing pressure needed to obtain a certain plasma density for the same laser conditions. Figure 6(a) shows the gas cell average density as a function of backing pressure for calibration measurements made throughout the experiment, and the calibration as a function of pump pulse shots with the cell in place is plotted in figure 6(b). It can be seen that the gradient of the calibration line decreases throughout the experiment, as the exit aperture sustained damage. The gas cell exit cone was replaced with a new cone before shots were taken for run 7. The gradient of the density calibration for this run (plotted in red) can be seen to return back to the initial value observed on run 1, for which the gas cell was undamaged.

The increase to the exit aperture diameter of the gas cell can also change the longitudinal density gradient [26], in addition to the observed change in average density. Although this was not measured directly, due to a limited field of view of the probe diagnostic, we can infer that the plasma density profile is affected by the aperture size from the LWFA performance. Figure 4 shows that a large increase in performance is seen when using the new exit aperture when compared to an exit aperture widened by laser damage. This was observed even though the laser conditions and average plasma densities were the same in each case.

This is also evident in the electron spectra, which show a dramatic reduction in total electron beam charge with the widened aperture. The comparison of the electron and x-ray properties before and after the gas cell exit aperture change are summarised in table 1. Although the x-ray critical energy and average electron energy are slightly higher with the new cell, the most significant changes when switching between the two cells were the electron beam charge and x-ray signal, which both increased by a factor of ≈ 2.

6. Conclusion

A compact x-ray imaging source capable of imaging centimetre scale objects was demonstrated. At the optimal plasma density, a bright x-ray source was generated with a maximum of 6×10^9 photons above 1 keV in a single shot with an on-axis synchrotron spectra with a critical energy of 13.8 keV. This x-ray source allowed imaging with a resolution of 4 μm $\times$ 5 μm at 10 $\times$ magnification. The imaging resolution was limited by the source radius and length, which were inferred to be 0.5 $\pm$0.2 μm $\times$ 3.2 $\pm$0.9 mm, as well as the camera pixel size and scintillator point-spread-function. Damage to the exit aperture of the gas cell, which caused changes to the plasma density profile, was shown to be detrimental to x-ray flux. It is essential that this is considered in the design of gas cells when working with higher repetition rate lasers for applications where they are required to operate at consistent performance levels for extended periods of time. Further experimentation on the tailoring of the longitudinal and transverse plasma density profiles [27] could potentially reduce the emission length, allowing for high resolution imaging over a wider angular range, while also enhancing the x-ray flux and spectrum.

Data availability statement

The data that support the findings of this study are available upon reasonable request from the authors.

Acknowledgments

The authors are very grateful for the hard work of the staff at the Central Laser Facility and for making this work possible. The Cockcroft Institute acknowledges support by STFC UK [ST/P002056/1]. The John Adams Institute acknowledges support by STFC, UK [ST/P002021/1] and by the EU Horizon 2020 research and innovation programme Grant No. 653782. C T was supported by an Engineering and Physical Sciences Research Council (EPSRC), UK Innovation Fellowship grant [EP/S001379/1]. A G R T acknowledges support by US DOE Grant DE-SC0020237.

ORCID iDs

O J Finlay https://orcid.org/0000-0002-0026-6584
J-N Gruse https://orcid.org/0000-0002-4099-8341
C Thornton https://orcid.org/0000-0003-1267-5788
C D Armstrong https://orcid.org/0000-0002-0157-3746
C D Baird https://orcid.org/0000-0001-9973-7173
S Cipiccia https://orcid.org/0000-0002-3485-2856
S P D Mangles https://orcid.org/0000-0003-2443-4201
C D Murphy https://orcid.org/0000-0003-3849-3229

Z Najmudin https://orcid.org/0000-0001-6323-4005
L R Pickard https://orcid.org/0000-0002-6878-9891
M P Selwood https://orcid.org/0000-0002-9163-1857
C I D Underwood https://orcid.org/0000-0002-1691-6377
A G R Thomas https://orcid.org/0000-0003-3206-8512
M J V Streeter https://orcid.org/0000-0001-9086-9831

References

[1] Tajima T and Dawson J M 1979 *Phys. Rev. Lett.* **43** 267
[2] Mangles S *et al* 2004 *Nature* **431** 535
[3] Geddes C G R, Toth C, van Tilborg J, Esarey E, Schroeder C B, Bruhwiler D, Nieter C, Cary J and Leemans W P 2004 *Nature* **431** 538 E
[4] Faure J, Glinec Y, Pukhov A, Kiselev S, Gordienko S, Lefebvre E, Rousseau J P, Burgy F and Malka V 2004 *Nature* **431** 541 E
[5] Thomas A G R 2010 *Phys. Plasmas* **17** 056708
[6] Albert F and Thomas A 2016 *Plasma Phys. Control. Fusion* **58** 103001
[7] Pukhov A and ter Vehn M 2002 *Appl. Phys.* B **74** 355
[8] Lu W, Tzoufras M, Joshi C, Tsung F S, Mori W B, Vieira J, Fonseca R A and Silva L O 2007 *Phys. Rev. ST Accel. Beams* **10** 061301
[9] Dawson J M 1959 *Phys. Rev.* **113** 383
[10] Esarey E, Schroeder C B and Leemans W P 2009 *Rev. Mod. Phys.* **81** 1229
[11] Fourmaux S *et al* 2011 *New J. Phys.* **13** 033017
[12] Rousse A *et al* 2004 *Phys. Rev. Lett.* **93** 135005
[13] Kneip S *et al* 2010 *Nat. Phys.* **6** 980
[14] Esarey E, Shadwick B A, Catravas P and Leemans W P 2002 *Phys. Rev.* E **65** 056505
[15] Corde S, Ta Phuoc K, Lambert G, Fitour R, Malka V, Rousse A, Beck A and Lefebvre E 2013 *Rev. Mod. Phys.* **85** 1
[16] Jackson J D 1999 *Classical Electrodynamics* 3rd edn (New York, NY: Wiley)
[17] Cole J M *et al* 2015 *Sci. Rep.* **5** 13244
[18] Cole J M *et al* 2018 *Proc. Natl Acad. Sci.* **115** 6335
[19] Gruse J-N *et al* 2020 *Nucl. Instrum. Methods Phys. Res.* A **983** 164369
[20] Hussein A E *et al* 2019 *Sci. Rep.* **9** 3249
[21] Takeda M, Ina H and Kobayashi S 1982 *J. Opt. Soc. Am.* **72** 156
[22] Madjarova V, Kadono H and Toyooka S 2003 *Opt. Express* **11** 617
[23] Bloom M S *et al* 2020 *Phys. Rev. Accel. Beams* **23** 061301
[24] JIMA (available at: https://www.jima.jp/content/pdf/catalog_rt_rc02b_eng.pdf)
[25] Corde S *et al* 2011 *Phys. Rev. Lett.* **107** 215004
[26] Kononenko O *et al* 2016 *Nuc. Instrum. Methods Phys. Res.* A **829** 125
[27] Kozlova M *et al* 2020 *Phys. Rev.* X **10** 011061